Genesis of Hurricane Julia (2010) within an African Easterly Wave: Developing and Nondeveloping Members from WRF–LETKF Ensemble Forecasts

STEFAN F. CECELSKI AND DA-LIN ZHANG

Department of Atmospheric and Oceanic Science, University of Maryland, College Park, College Park, Maryland

TAKEMASA MIYOSHI

RIKEN Advanced Institute for Computational Science, Kobe, Japan

(Manuscript received 24 June 2013, in final form 30 December 2013)

ABSTRACT

In this study, the predictability of and parametric differences in the genesis of Hurricane Julia (2010) are investigated using 20 mesoscale ensemble forecasts with the finest resolution of 1 km. Results show that the genesis of Julia is highly predictable, with all but two members undergoing genesis. Despite the high predictability, substantial parametric differences exist between the stronger and weaker members. Notably, the strongest-developing member exhibits large upper-tropospheric warming within a storm-scale outflow during genesis. In contrast, the nondeveloping member has weak and more localized warming due to inhibited convective development and a lack of a storm-scale outflow. A reduction in the Rossby radius of deformation in the strongest member aids in the accumulation of the warmth, while little contraction takes place in the nondeveloping member. The warming in the upper troposphere is responsible for the development of meso-α-scale surface pressure falls and a meso-β surface low in the strongest-developing member. Such features fail to form in the nondeveloping member as weak upper-tropospheric warming is unable to induce meaningful surface pressure falls. Cloud ice content is nearly doubled in the strongest member as compared to its nondeveloping counterparts, suggesting the importance of depositional heating of the upper troposphere. It is found that the stronger member undergoes genesis faster due to the lack of convective inhibition near the African easterly wave (AEW) pouch center prior to genesis. This allows for the faster development of a mesoscale convective system and storm-scale outflow, given the already favorable larger-scale conditions.

1. Introduction

Tropical cyclogenesis (TCG), the transition of a nonintensifying tropical disturbance into an intensifying one, is characterized by a plethora of processes ranging across numerous spatial scales. These processes are some of the least understood in the field of tropical meteorology today, leading to deficiencies in predicting when and where TCG will take place. Recent research has expanded on the roles of multiscale interactions in TCG, signifying the importance of both mesoscale features [such as mesoscale convective systems (MCSs)] and synoptic-scale phenomena [such as African easterly waves (AEWs)]. Even with such advances, our understanding of TCG and its predictability are limited due to the lack of observational data at the places where TCG occurs and the need for computationally intensive high-resolution numerical model predictions.

Of particular relevance to this study are the recent advances made in relation to TCG within an AEW, that is, the roles of the latter in TCG. Specifically, the marsupial pouch paradigm (Dunkerton et al. 2009; Wang et al. 2010a; Montgomery et al. 2010) provides a theoretical construct that describes the ideal location for a meso-β-scale low-level vortex (LLV) to develop within an AEW (Cecelski and Zhang 2013). Within this mindset, the AEW serves as the parent to the developing LLV, protecting it from adverse environmental conditions. The Pre-Depression Investigation of Cloud-Systems in the Tropics (PREDICT; Montgomery et al. 2012) field campaign used the marsupial pouch paradigm to diagnose developing and nondeveloping AEWs during the 2010 North Atlantic hurricane season with

Corresponding author address: Dr. Da-Lin Zhang, Department of Atmospheric and Oceanic Science, University of Maryland, College Park, College Park, MD 20742.
E-mail: dalin@atmos.umd.edu

DOI: 10.1175/JAS-D-13-0187.1

promising preliminary results. Other studies have taken a different approach to understanding the role of the AEW during TCG. Differences between nondeveloping and developing AEWs have been demonstrated by Hopsch et al. (2010) and Dunkerton et al. (2009), who conclude that the persistence of deep convection, tropospheric moisture content, and low-level vorticity growth are all important for an AEW to develop a tropical depression (TD).

The marsupial pouch paradigm assumes the bottom-up growth of TD-scale cyclonic vorticity (Zhang and Bao 1996; Hendricks et al. 2004; Montgomery et al. 2006), the development of vortical hot towers (VHTs) as the building blocks of tropical cyclones (TCs; Hendricks et al. 2004; Montgomery et al. 2006), and the aggregation of VHTs into the LLV (Hendricks et al. 2004; Montgomery et al. 2006; Sippel et al. 2006; Houze et al. 2009). More recently, it has been shown that convective development and the aggregation of mesovortices are more likely to occur along the AEW low-level critical latitude[1] (Dunkerton et al. 2009; Cecelski and Zhang 2013). In addition, Zhang and Zhu (2012) and Cecelski and Zhang (2013) promote the importance of meso-α-scale upper-tropospheric warming during TCG in conjunction with bottom-up vorticity growth. Results indicate that the upper-tropospheric warming develops as a result of heating due to depositional growth and freezing from deep convection and subsequent advection by divergent outflow beyond the Rossby radius of deformation (L_R). This warming may hydrostatically induce meso-α mean sea level pressure (MSLP) falls, which help strengthen the development of meso-β-scale LLVs through enhanced convergence in the planetary boundary layer (PBL).

While the majority of the previous discussion has elaborated upon TCG through modeling and observational studies, very little work has investigated TCG using a particular niche of modeling studies: ensemble simulations. A notable study of Sippel and Zhang (2008), who conducted short-range ensemble forecasts on a nondeveloping tropical disturbance in the Gulf of Mexico during the 2004 North Atlantic hurricane season, assessed the differences between ensemble members using a linear correlation to generate statistical sensitivities of storm intensity changes to specific meteorological parameters. Dynamical differences between ensemble members were then inferred from these sensitivities. The work discovered that the presence of deep moisture and high convective available potential energy (CAPE) are the two most important factors in the initial conditions (ICs), which combine to yield a more active spinup in the first 6–12 h of integration. Beyond this spinup period, they demonstrated that the ensemble spread increased due to the differences in convection and the wind-induced surface heat exchange (WISHE; Emanuel et al. 1994) mechanism that some members utilized. Snyder et al. (2010) investigated the National Centers for Environmental Prediction (NCEP) global ensemble forecast system in predicting the TCG and evolution of five TCs and two nondeveloping systems during the National Aeronautics and Space Administration (NASA) African Monsoon Multidisciplinary Analyses (NAMMA). They found that the ensemble system predicted TCG of three strong storms that formed within AEWs, but failed to predict TCG for two weaker storms. Their study suggested that the accuracy of TCG forecasts from the global ensemble was 50% for forecasts initialized in the pregenesis phase. In addition, Enomoto et al. (2010) found that the ensemble spread increased prior to TCG, as the ensemble solutions diverged in the intensity and timing of TCG.

The objectives of the present study are to (i) compare and contrast the simulated TCG of Hurricane Julia (2010) between the control simulation using the Weather Research and Forecasting Model (WRF) (Skamarock et al. 2005) and the ensemble simulations using the coupled WRF and local ensemble transform Kalman filter (LETKF) system (Hunt et al. 2007; Miyoshi and Kunii 2012, hereafter MK12); and (ii) identify the fundamental synoptic-scale and mesoscale differences between developing and nondeveloping ensemble members, or developers and nondevelopers for short, with an emphasis on upper-level warming (Zhang and Zhu 2012; Cecelski and Zhang 2013), the outflow layer, and convective development. The objectives are achieved through 66 h, cloud-resolving simulations of the TCG of Hurricane Julia from 20 ensemble members and a control using the finest 1-km horizontal resolution.

The next section describes the WRF–LETKF system, the method for perturbing the ICs, and the WRF setup. Section 3 discusses the overall intensity and track results from the ensemble simulations, including the identification of developers and nondevelopers. Section 4 compares and contrasts the developers and nondevelopers members with respect to differences in synoptic and mesoscale features, focusing on upper-level warming, the upper outflow layer, and convective development.

2. Model setup

The WRF–LETKF system (MK12) is used herein because of the successful applications of the LETKF

[1] The critical latitude is defined as the latitude where the zonal wind speed equals the phase speed of the AEW at a particular level.

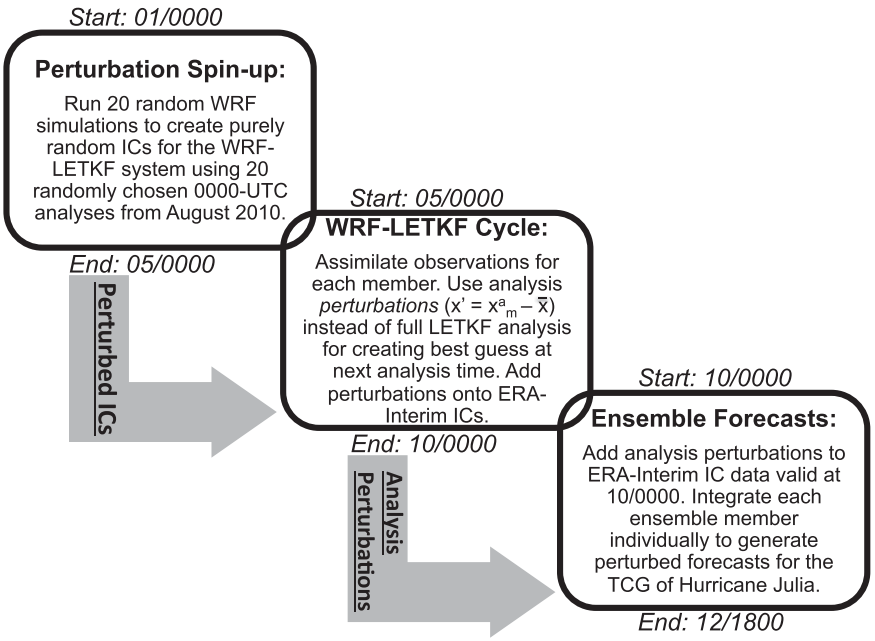

FIG. 1. Flowchart of the major steps of the ensemble forecast process. The perturbed ICs are created by the perturbation spinup step, which starts and ends at 01/0000 and 05/0000, respectively. The WRF–LETKF assimilation cycle is then run for 96 h, terminating at 10/0000. At this time, the 10/0000 analysis perturbations (x') are created by calculating the differences between the ensemble-mean ($\overline{x}$) and each member's analysis (x^a_m, where a represents analysis and m represents each ensemble member, ranging from 1 to 20). The 66-h ensemble forecasts are independently integrated forward to 12/1800, at which time Julia is declared a TS.

system to other numerical weather prediction models, including the Japan Meteorological Agency (JMA) operational model (Miyoshi et al. 2010). While creating the ensemble forecasts from the perturbed initial conditions, we strive for consistency with the control simulation and its parameterizations, as outlined in the next subsection.

a. WRF–LETKF assimilation cycle

Figure 1 shows the step-by-step approach to generating the ensemble forecasts of Hurricane Julia. The first step is referred to as the ''perturbation spinup,'' which creates randomly perturbed ICs for the WRF–LETKF system. Specifically, European Centre for Medium-Range Weather Forecasts (ECMWF) Re-Analysis (ERA-Interim) from 0000 UTC for 20 randomly selected days in the month of August 2010 are used to initialize this spinup period in order to keep the dynamical consistency with the large-scale flows characteristic of the 2010 North Atlantic hurricane season. Each of the 20 random analyses is treated as ''the analysis'' of 0000 UTC 1 September (referred hereafter to as 1/0000), which is 96 h before the WRF–LETKF cycle begins. Using these random ICs, 20 separate WRF forecasts are integrated forward from 1/0000 to 5/0000, creating randomly perturbed initial conditions for ingestion into the WRF-LETKF system. This approach follows closely that used by MK12, whose randomly created ICs showed promising results with a similar length spinup.

The second step in Fig. 1 is the WRF-LETKF assimilation cycle, which begins at 5/0000 and is run for 96 h until 10/0000, at which time the initialization of the control simulation (Cecelski and Zhang 2013) is valid. Note that an assimilation cycle is needed here because the ''analyses of 5/0000'' from step one are obtained by integrating from 20 randomly selected ICs. In this study, the assimilation cycle uses observational data from NCEP's operational Global Data Assimilation System (GDAS); see the appendix for more details. The main goal here is to generate realistic perturbations of the atmospheric state at a time just prior to the TCG of Julia. Using these perturbations, ensemble forecasts will yield a spread of solutions of TCG, which are then investigated to identify the fundamental processes (and related perturbations) responsible for the evolution of the disturbance into TD Julia.

For step two, a single 27-km-resolution domain is centered on the region of interest (LETKF; Fig. 2) with the WRF–LETKF system creating analyses every 6 h over the 96-h period. The relevant WRF parameterizations

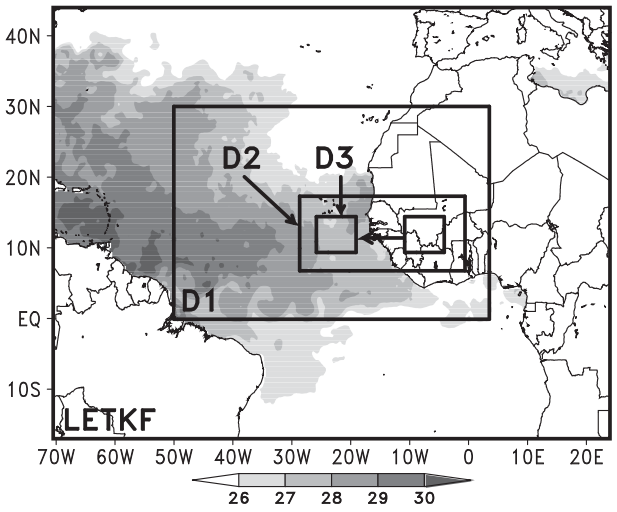

FIG. 2. WRF domain setup for both the WRF–LETKF cycle (LETKF) with a horizontal resolution of 27 km and the subsequent nested forecast domains of D1, D2, and D3 with the horizontal resolutions of 9, 3, and 1 km, respectively. Domain D3 is a moving one with the starting and ending positions marked by the respective boxes. The NOAA OI SST data are shaded at intervals of 1°C.

used in the assimilation cycle include (i) the WSM five-class cloud microphysics scheme (Hong et al. 2004); (ii) the Kain–Fritsch convective scheme (Kain 2004); (iii) the Rapid Radiative Transfer Model (RRTM) longwave radiation scheme (Mlawer et al. 1997); (iv) the Dudhia shortwave radiation scheme Dudhia (1989); and (v) the Yonsei University (YSU) PBL scheme (Noh et al. 2003). All 20 members are given the same boundary conditions, which come from 6-hourly ERA-Interim. Even though the members are identical at the boundaries using this method, substantial differences between the members do exist in the central region of the domain, as was also found by MK12.

A significant difference between the assimilation cycle used herein and by MK12 revolves around how the WRF–LETKF ensemble analyses are used in the cycle. MK12 overwrites the initial conditions from the WRF preprocessing system (WPS) with the WRF–LETKF system analyses, leaving the WPS-created boundary conditions intact for each assimilation period. In contrast, the current study creates initial and lateral boundary conditions from ERA-Interim using WPS, but only uses the analysis perturbations for each ensemble member (e.g., $x_t'^{(m)} = x_t^{a(m)} - \overline{x}_t^a$, where m is the ensemble member, a stands for analysis, and t represents the analysis time) from the WRF-LETKF system. These perturbations are added to the WPS-processed ERA-Interim initial conditions (which are deterministic in nature), creating perturbed initial conditions for the next assimilation period. Given that the main goal of running the WRF–LETKF cycle is to generate realistic perturbations of the atmospheric state, it is unnecessary to keep the full analysis of each ensemble member. This rationale results in the ensemble perturbations being added to the ERA-Interim data for each 6-hourly analysis period. Obviously, the ensemble perturbations at 10/0000 are of the utmost importance since these perturbations create a spread of perturbed initial conditions centered on the control simulation, which is initialized from the 10/0000 ERA-Interim data. Our method "recenters" the ensemble perturbations about ERA-Interim every 6 h, and thus, the perturbations are nearly in balance with ERA-Interim in addition to the ensemble mean. To ensure proper balance (and centering) of the perturbations, the ensemble-mean analysis is compared to the ERA-Interim at various times, including 10/0000 (not shown). These comparisons reveal that both analyses are nearly identical with horizontal resolution being the only notable difference (e.g., 27 km vs 0.7° for WRF–LETKF and ERA-Interim, respectively).

b. *Ensemble forecast integration*

The WRF–LETKF-generated (perturbed) ICs are integrated 66 h forward to 12/1800 to produce ensemble forecasts for the TCG of Hurricane Julia, whose output can be compared with the control simulation discussed in Cecelski and Zhang (2013). These ensemble forecasts are made using the same domain and model physics setup as the control, but with the addition of the 27-km-resolution domain. The WRF–LETKF domain (LETKF; Fig. 2) supplies the initial and lateral boundary conditions to the inner domains, having the same 9-, 3-, and 1-km horizontal resolutions as the control simulation (D1, D2, and D3, respectively; Fig. 2). The lateral boundary conditions of the 27-km-resolution domain are supplied by the ERA-Interim like the assimilation cycle. The sea surface temperatures (SSTs) are supplied by the National Oceanic and Atmospheric Administration (NOAA) Optimal Interpolation (OI) high-resolution SST dataset (Reynolds et al. 2007) valid at 10/0000, keeping consistency with the control simulation. The only difference in the WRF setup from the assimilation cycle is the use of the Thompson graupel two-moment (Thompson et al. 2008) microphysics scheme, the same scheme used in the control simulation.

3. WRF–LETKF cycle and ensemble forecast results

Before examining in-depth the results from the ensemble forecasts, it is fruitful to examine some characteristics of the WRF–LETKF cycle in addition to the track and intensity results from the ensemble as a whole.

For the remainder of this paper, TCG is defined in the same fashion as that described in Cecelski and Zhang (2013), that is, the time at which a closed MSLP isobar of sufficient size and intensity on the standard 4-hPa contouring interval occurs. This time will be assessed in comparison to the time the National Hurricane Center (NHC) declared Hurricane Julia a TD, 12/0600 [named a tropical storm (TS) 12 h later]. Prior to this time is herein referred to as TCG, while after is referred to as the significant intensification (SI) period. Because of the above definition for TCG, MSLP rather than the relative vorticity field will be used to examine the intensity of the ensemble-simulated storms.

a. Results from the WRF–LETKF cycle

Unlike other data assimilation studies that strive to quantify and thoroughly describe the performance of the data assimilation system, we are more concerned with the creation of realistic ensemble perturbations. To this end, Fig. 3 shows the domain-averaged analysis spread at $\sigma = 0.597\,12$ (approximately 600 hPa) for u, v, T, and q_v from 05/0600 to 10/0000. This level is used to examine ensemble spread because near it the AEW cyclonic vorticity and related circulation field are maximized prior to TCG (Cecelski and Zhang 2013). The ensemble spread of all variables decreases rapidly during the first 12 h of integration and then remains nearly constant, with further decreases during the last 6-h assimilation period, alluding to the creation of reasonable flow-dependent ensemble perturbations. The ensemble spread of approximately 0.4 m s^{-1} for u (Fig. 3a) is consistent with experiments using both adaptive and globally constant multiplicative inflation in MK12.

b. Ensemble forecast track and intensity

The tracks from the 20-member ensemble forecasts are shown in Fig. 4, as compared to the control simulation (black, squares) and best fixes from the NHC (black, circles). The same tracking methodology as that in Cecelski and Zhang (2013) is used, with the track initially being generated using 600- and 700-hPa circulation centers in conjunction with large absolute vorticity. The tracking is then shifted to the central minimum pressure (P_{MIN}) center of sufficient spatial size once it forms. This transition varies between ensemble members and could lend to some of the track spread seen in Fig. 4.

Overall, the track of the AEW prior to coastal transition is well agreed upon by nearly all members, with the majority of the track differences occurring near the end of the 66-h simulation. Interestingly, the outlying southernmost solution after coastal transition is the control

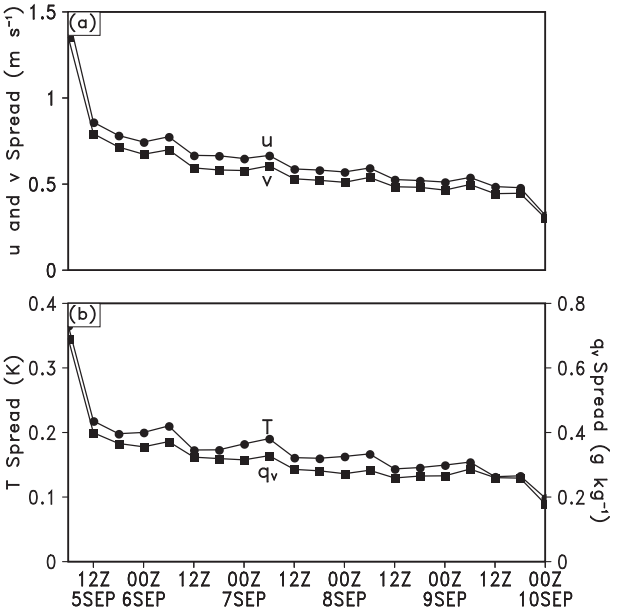

FIG. 3. Time series of ensemble spreads during the period from 0600 UTC 5 Sep to 0000 UTC 10 Sep 2010 for (a) the zonal wind (u, m s^{-1}) and meridional wind (v, m s^{-1}) and (b) temperature (T, °C) and water vapor mixing ratio (q_v, g kg^{-1}) at $\sigma = 0.597\,12$, approximately 600 hPa, averaged over the entire WRF–LETKF domain shown in Fig. 2.

simulation, with an overall track error of 173 km as compared to the best fixes. The ensemble-mean track improves upon the control simulation by over 40 km, with a mean track error of 131 km, while the member with the best track has an average track error of just 106 km. Substantial variability in the track exists after 12/0600, which is in agreement with the strength differences of the forecast storms among the ensemble members to be shown in the next.

Figure 5 shows the time series of the storm intensities in terms of P_{MIN} and 10-m maximum sustained wind speed (V_{MAX}) from the 20 ensemble members, control simulation (black, squares), and NHC-estimated intensity (black, circles). Additionally, the ensemble spreads for P_{MIN} and V_{MAX} are also plotted in terms of sample standard deviation (dashed lines). Obviously, the ensemble spread of each parameter increases as the integration progresses, reaching maximums of approximately 2.5 hPa and 4 m s^{-1}, respectively, at 12/1800. Out of the 20 members, 18 members produce P_{MIN} below 1007 hPa from the NHC-estimated P_{MIN} at 12/0600, while the remaining 2 members simulate a storm with P_{MIN} of 1007 hPa, agreeing with the NHC-estimated intensity. This large bias for a stronger storm at 12/0600 (with an ensemble-mean P_{MIN} of 1004 hPa) hints at the possibility that the NHC-estimated intensity is too weak by 2–3 hPa, but such a difference is probably within the

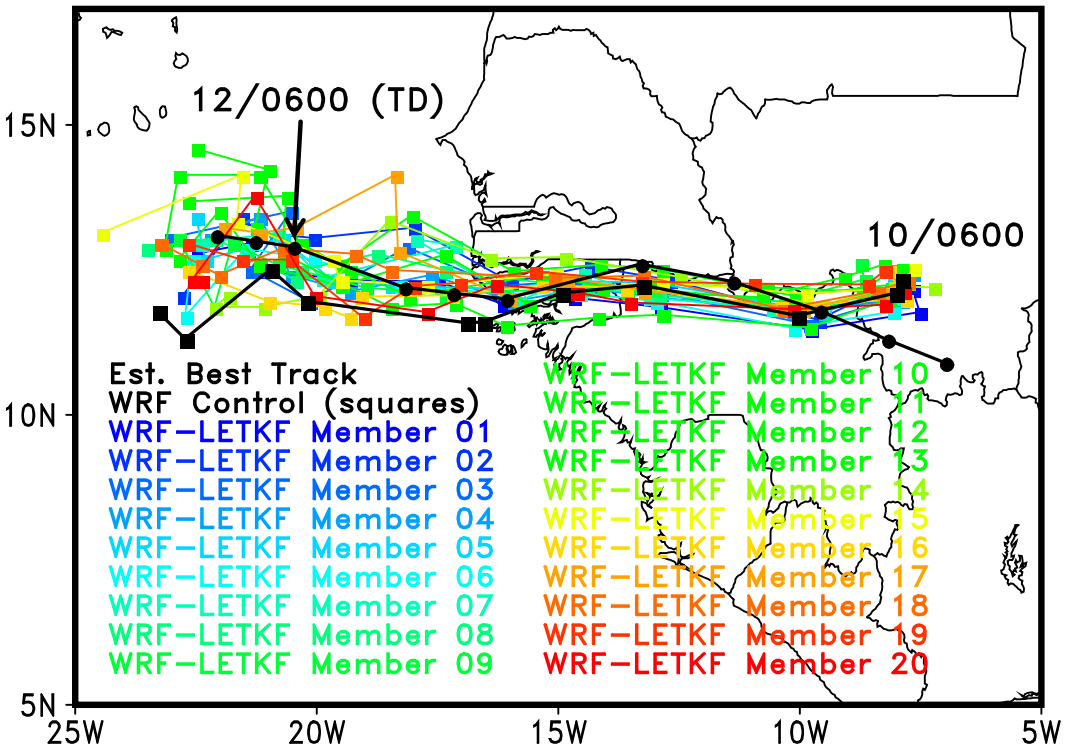

FIG. 4. Tracks of each WRF–LETKF ensemble member (colored by member) as compared to the control simulation (black, squares) and best NHC-estimated (black, circles) tracks valid from 0600 UTC 10 Sep to 1800 UTC 12 Sep 2010.

range of accepted error. About 16 out of the 20 members are stronger than 1005 hPa at 12/1800, with the strongest member reaching a P_{MIN} of 999 hPa. In contrast, 2 out of the 20 members are weaker than 1005 hPa at 12/1800, while the final 2 members have the same NHC estimate of 1005 hPa. Thus, we may state that the TCG of Hurricane Julia is highly predictable in terms of P_{MIN}, with nearly all members depicting a TD-like intensity at 12/0600 and a TS-like intensity at 12/1800.

c. *Selection of developers and nondevelopers*

Given the spread among the 20 members, it is desirable to examine which member reproduces the genesis of Julia too strongly or weakly, as well as which members have the best and worst track. Here, the best (and worst) track is selected using the overall average track error when compared to the NHC-estimated track. Similarly, the best (and worst) members for intensity are based purely on the members' P_{MIN}, as compared to the NHC-estimated P_{MIN}, in addition to the storm intensity when declared a TD and TS. We decide to use P_{MIN} rather than V_{MAX} to identify these members since its time series best defines the schism between developers and nondevelopers (see Fig. 5a). More attention will be given to the intensity of individual members rather than the track because TCG marks a distinction between intensity changes, not track changes.

Figure 6 shows the tracks and intensities for the member with the best track (member 4, orange) and the best intensity (member 7, green), as well as the member with the strongest storm (member 10, red) and weakest storm (member 14, blue). Member 7 compares favorably to the NHC (black circles), with an average absolute intensity error in P_{MIN} of 0.95 hPa. Further supporting its selection as the member who best replicates NHC estimates, member 7 has the same P_{MIN} as the NHC estimate at TD and TS times in conjunction with a total track error of 140 km.

In contrast to the "best" members, the member with the worst track error is also the member with the strongest overall storm (member 10, red line in Fig. 6). The overall track error of 246 km is significantly above the ensemble-mean and control track errors, with most of this track error occurring later in the integration. Of interest is the time series of P_{MIN} given in Fig. 6b, showing that member 10 (red) deepens 4.5 hPa between 11/1200 and 11/1800, reaching a P_{MIN} of 999 hPa at 12/1800. Contrasting member 10 is member 14, a nondeveloper (blue line), which never develops into a TD and ends the 66-h integration with a P_{MIN} of 1007 hPa at

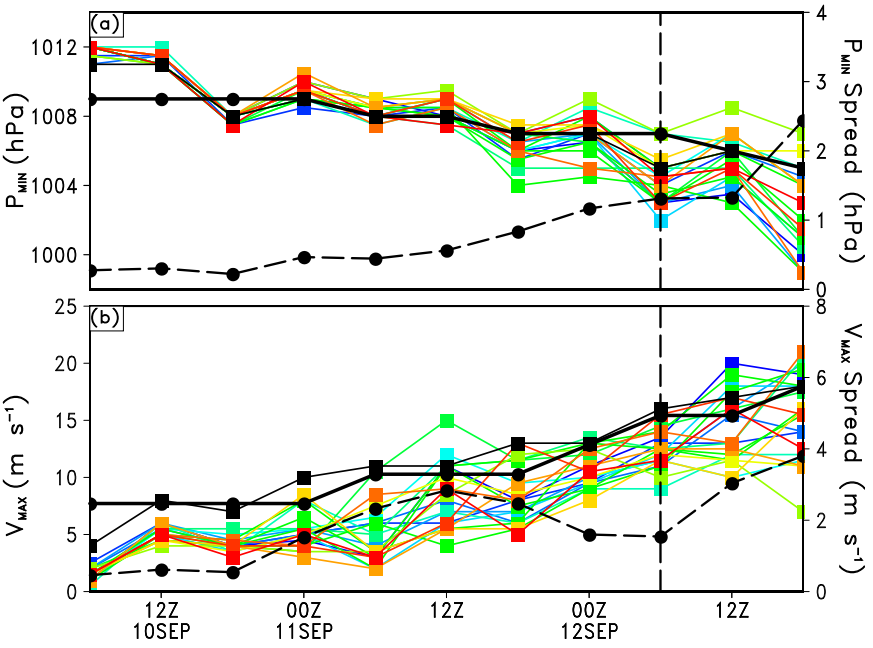

FIG. 5. Time series of the intensity of Hurricane Julia in terms of (a) P_{MIN} (hPa) and (b) V_{MAX} (m s^{-1}) from each WRF–LETKF member (colored by member), the control simulation (black, squares), and the NHC estimated (black, circles). The dashed lines with black circles represent the ensemble spread (i.e., sample standard deviation with right-hand y axis) of P_{MIN} and V_{MAX}, respectively. The vertical dashed lines represent the time of TCG as determined by NHC.

12/1800. Both members 10 and 14 are used in conjunction with member 7 and the control simulation to assess the dynamic and thermodynamic differences taking place during TCG.

The members of interest (7, 10, and 14) show differences with respect to spatial cloud patterns when compared to the observed *Meteosat-9* IR imagery (cf. Figs. 7 and 8). After 12 h into the integration (Figs. 8a,e,i,m), little differences exist between the members with minimal convective initiation. By 11/1200 (Figs. 8b,f,j,n), differences between the members start to emerge, but all fail to capture the large, round-shaped MCS found in the observed IR (Fig. 7b). At the time of TCG (Figs. 8c,g,k,o), only member 10 (the strongest developer) and the control simulation compare favorably with the observed *Meteosat-9* IR image (Fig. 7c). This supports our initial postulation that the NHC P_{MIN} estimate at 12/0600 might be too weak, since (i) the strongest member compares favorably to the observed cloud spatial patterns; and (ii) the member with comparable P_{MIN} to the NHC estimate (member 7) depicts weak, sporadic convection at the same time. By 12/1800, the two weaker members (Figs. 8d,l) depict a more coherent MCS, but do not exhibit the cyclonic circulation in the cloud fields seen in member 10 (Fig. 8h), the control simulation (Fig. 8p), and the observed (Fig. 7d). Overall, member 10 and the control simulation have the most realistic representation of the cloud field associated with the AEW and subsequent TS.

4. Parametric differences between ensemble members

To isolate what causes the intensity differences shown in the preceding section, we examine the differences between the developers and nondevelopers from a synoptic and mesoscale viewpoint. Of particular interest is the initiation of deep convection and its persistence during TCG, which have previously been studied by Sippel and Zhang (2008) and Hopsch et al. (2010) in terms of CAPE and tropospheric moisture content. In addition, we investigate the differences in upper-tropospheric processes, including upper-level warming and changes to the outflow layer, as previously emphasized by Zhang and Zhu (2012) and Cecelski and Zhang (2013).

a. Differences in the upper-level warming

Following Chen and Zhang (2013), Zhang and Zhu (2012), and Cecelski and Zhang (2013), Fig. 9 presents the time series of the area-averaged cloud ice content (10^{-4} g kg^{-1}) and relative warming with respect to the

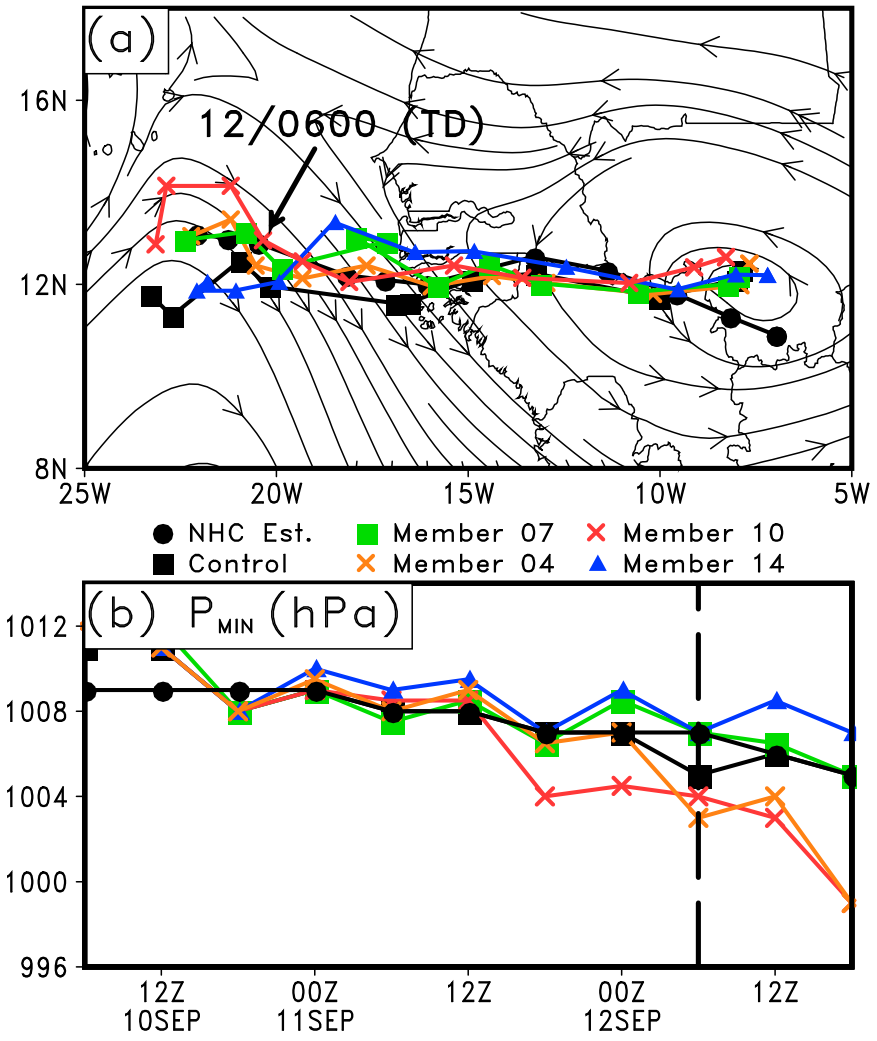

FIG. 6. (a) The tracks from the member with the best track (member 4, orange), best intensity (member 7, green), the weakest storm (member 14, blue), and the strongest storm (member 10, red) in comparison to WRF control simulated (black, squares) and NHC estimated (black, circles) superimposed with ERA-Interim 600-hPa comoving streamlines valid at 0600 UTC 10 Sep. (b) Time series of the P_{MIN} (hPa) of each of the members in relation to the WRF control-simulated and NHC best estimates. Colored lines in (b) have the same meaning as in (a). The vertical dashed line in (b) represents the time of TCG as estimated by NHC.

vertical temperature profile at 11/0600, at which time, all members have a distinct midlevel circulation associated with AEWs over land. The relationship between the warming aloft and surface pressure changes are shown in Fig. 10, with the 200-hPa temperatures greater than −53°C shaded and the MSLP field overlaid.

It is obvious that the two stronger storms have a burst of warming exceeding 1.5°C just before and at the onset of TCG (Figs. 9b,d). Prior to this burst, warming in excess of 0.5°C exists in the 500–150-hPa layer, beginning just after 11/1200. This warming layer deepens and intensifies in both member 10 and the control approaching their respective TCG times, with member 10 exhibiting warming in excess of 1.5°C at 11/1800 (Fig. 9b). The 11/1800 time also marks the first time when a distinguishable P_{MIN} is found in member 10, directly beneath a meso-β-scale area of temperatures exceeding −52.5°C at 200 hPa (Fig. 10b). In contrast, the control simulation shows a broad area of lower MSLPs over the ocean with no appreciable concentration of warmth at 200 hPa (Fig. 10d). Member 10 undergoes TCG first, warming over 0.5°C with an accumulation of high cloud ice content between 11/1800 and 12/0000 (Fig. 9b). During this period, an expansion of the warmth at 200 hPa over the meso-α-scale occurs due to the development of a storm-scale outflow. This meso-α area of warmer temperatures

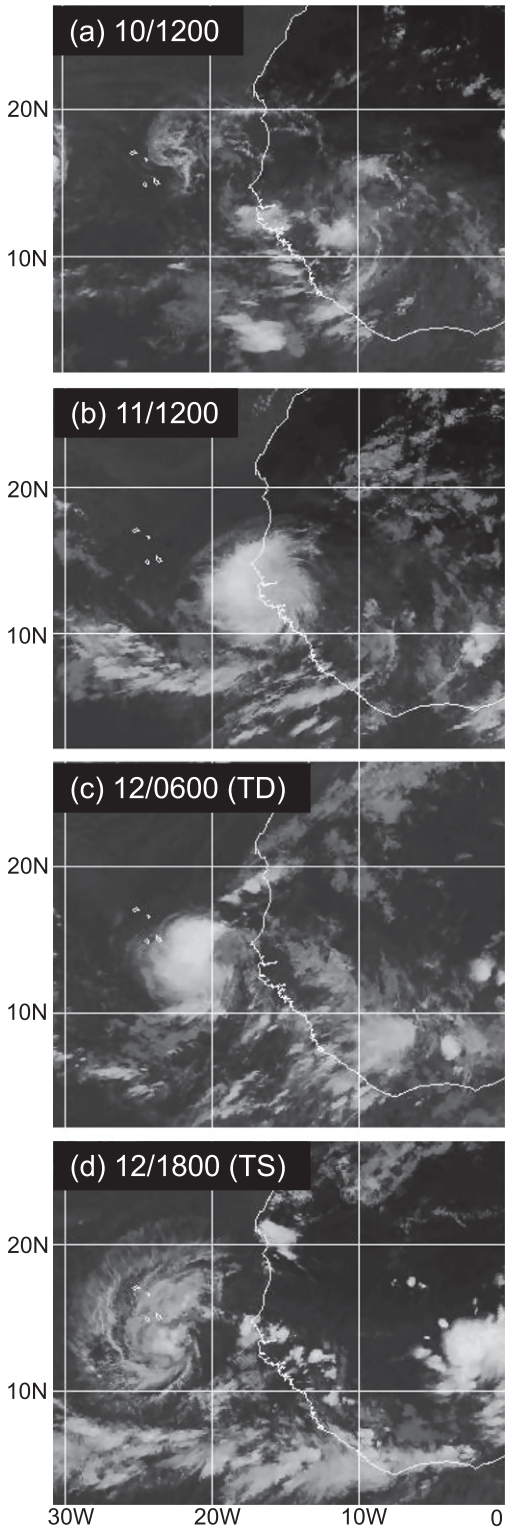

FIG. 7. *Meteosat-9* IR imagery at various stages of Hurricane Julia's evolution: (a) sporadic convection within the AEW at 1200 UTC 10 Sep, (b) well-defined MCS within the AEW at 1200 UTC 11 Sep, (c) TD at 0600 UTC 12 Sep, and (d) TS at 1800 UTC 12 Sep. Adapted from Fig. 4 of Cecelski and Zhang (2013).

hydrostatically induces similar-sized MSLP falls, while directly beneath the warmest 200-hPa temperatures the meso-β P_{MIN} seen in Fig. 10b intensifies into the TD in Fig. 10f.

The control-simulated storm undergoes TCG between 12/0000 and 12/0600, with an increase in the upper-level warming from 0.75°C to in excess of 1.5°C, combined with an accumulation of large cloud ice content (Fig. 9d). In a fashion similar to member 10, the control also shows the development of a meso-β-scale P_{MIN} beneath 200-hPa temperatures between −53° and −52.5°C (Fig. 10h). This warming expands markedly in a region characterized by storm-scale outflow, inducing MSLP falls on a meso-α-scale area in addition to generating the meso-β surface low (TD Julia) at 12/0600 (Fig. 10l).

After their respective TCG, both member 10 and the control simulation depict a weakening of warming within 100 km of the storm center, followed by a restrengthening toward the end of the simulations (Figs. 9b,d). This weakening is more apparent in the control, with the 200-hPa temperatures in excess of −52.5°C contracting between 12/0600 and 12/1800 (Figs. 10p,t). An increase in vertical wind shear (VWS) to between 8 and 12 m s^{-1} in the 400–100-hPa layer (Fig. 11c) in the control can partially explain the weakening of the warming. Meso-α MSLP falls at the surface continue between 12/1200 and 12/1800 in member 10, with the warmest regions at 200 hPa characterized by a meso-β-scale surface low present directly beneath (Figs. 10n,r). At 12/1800, temperature differences again intensify to greater than 1.5°C (Fig. 9b), with a 999-hPa TS-like meso-α surface low directly beneath the warm region at 200 hPa (Fig. 10r).

On the other hand, the two weakest members struggle to develop such significant upper-level warming (Figs. 9a,c). For example, the majority of the time series of member 7, which is the best as compared to NHC estimates, is dominated by sporadic meso-β-scale warming less than 1.0°C with cloud ice content less than half that of the strongest developer. It is not until just prior to 12/1200 that persistent warming develops in a layer between 600 and 150 hPa, with a notable increase in cloud ice content over the same depth. This warming intensifies by the end of the simulation, finally reaching 1.25°C between 12/1200 and 12/1800, undergoing TCG. Such sporadic warming prior to 12/1200 supports the lack of a persistent P_{MIN} center (Figs. 10a,e,i), since the warming is unable to hydrostatically induce mesoscale MSLP falls. This inability can be attributed to the lack of a storm-scale outflow in contrast to the stronger developers, among other attributes shown in following sections (cf. Figs. 10e and 10f).

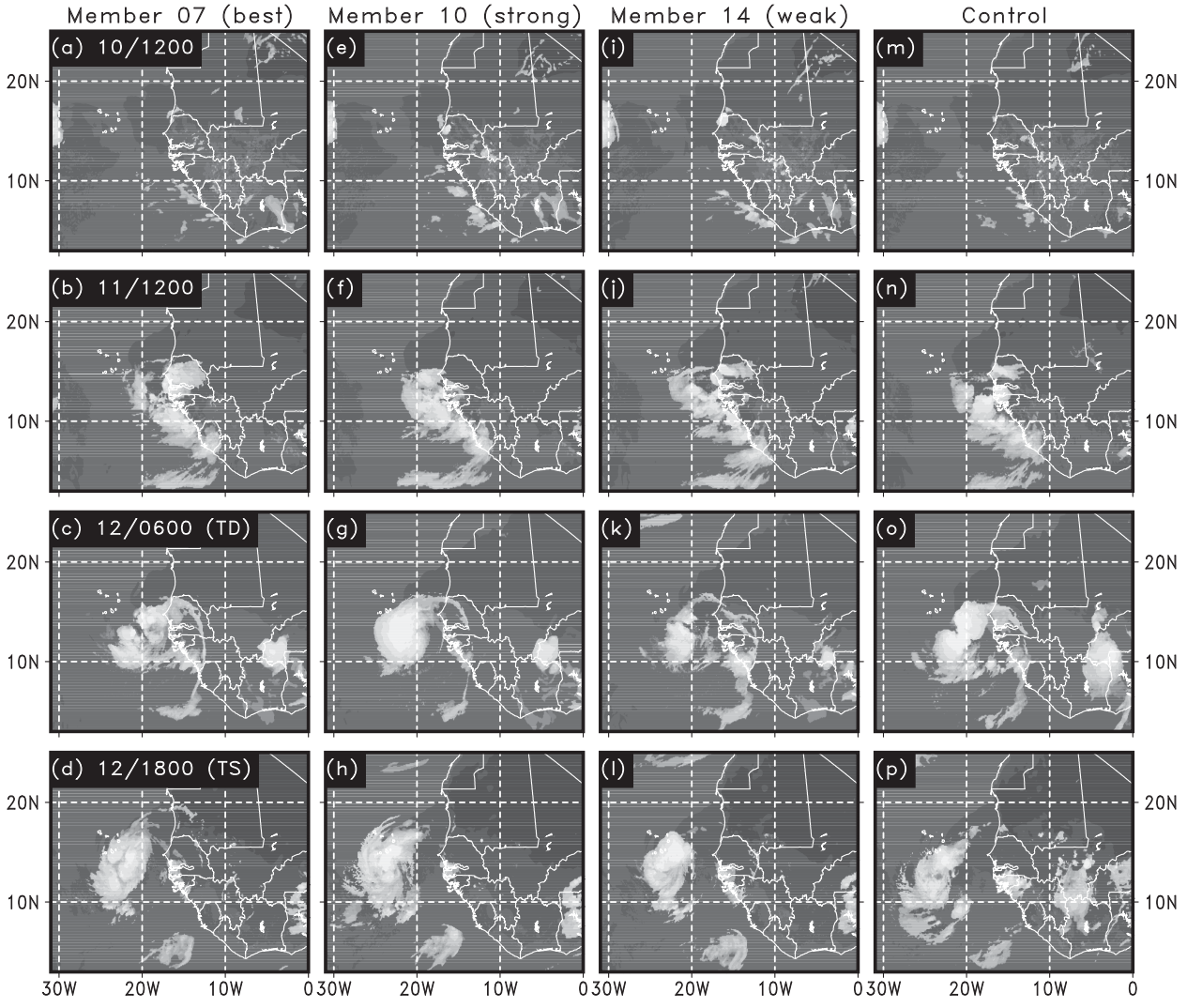

FIG. 8. Comparison of WRF-derived brightness temperature (K) from members (a)–(d) 7 (best intensity), (e)–(h) 10 (strongest developer), (i)–(l) 14 (nondeveloper), and (m)–(p) from the control simulation at the same times as in Fig. 7. Data from the 9-km-resolution simulation were used.

Member 14 is unique in that persistent warming in excess of 0.5°C in association with moderate cloud ice content between 500 and 200 hPa exists for just over a 24-h period, but a TD never develops (Fig. 9c). The core of this warming exceeds 0.75°C from approximately 11/1800 to 12/0600 (Fig. 9c), with an identifiable meso-β-scale P_{MIN} evident beneath the warmest temperatures at 200 hPa (Figs. 10c,g,k). The warmest temperatures are localized, however, inhibiting the growth of a TD-scale P_{MIN}. The presence of a weak storm-scale outflow suppresses the expansion of the warmth resulting in minimal meso-α-scale MSLP falls. After 12/0600, the warming near the storm center weakens below 0.75°C (Fig. 9c) with a similar response seen in the 200-hPa temperature field (Figs. 10o,s).

Since we have identified meaningful differences in MSLP and upper-tropospheric temperatures from the four selected simulations, it is worthwhile to see if the differences also exist in the ensemble as a whole. To this end, Fig. 11 compares the area-averaged 400–150-hPa layer-averaged temperatures and MSLP among all the ensemble members; the former parameter is chosen based on the general depth of the warming layer of the four storms in Fig. 9. It is evident that the majority of members at 12/0000 have area-averaged MSLP between 1010 and 1009 hPa, with corresponding upper-tropospheric temperatures at or below −37°C (Fig. 11a). A clear, negative relationship, with a correlation coefficient of −0.768, exists between the parameters, alluding to members with warmer upper-tropospheric temperatures

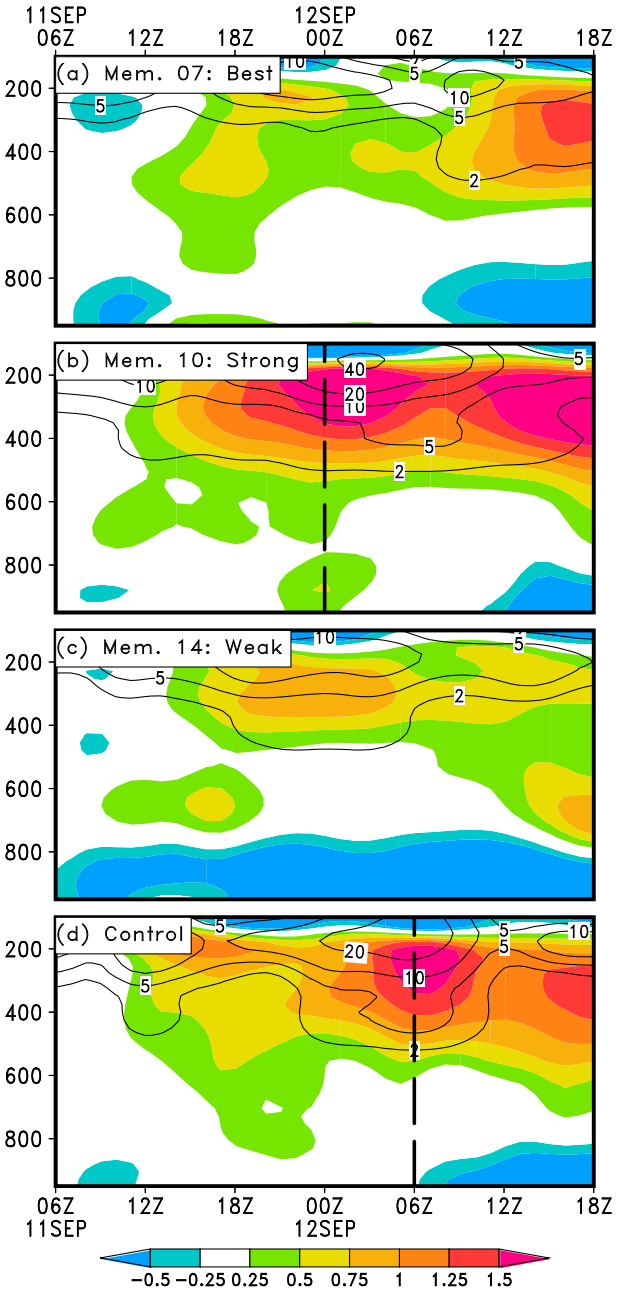

FIG. 9. Time–height cross sections of the temperature differences from the 30-h simulated values (valid at 0600 UTC 11 Sep, color shaded, °C) and cloud ice mixing ratio (contoured at 2, 5, 10, 20, and 40 × 10^{-4} g kg^{-1}) averaged over an area of 100 km × 100 km surrounding the storm center from hourly 3-km-resolution domains associated with members (a) 7 (best), (b) 10 (strongest developer), (c) 14 (nondeveloper), and (d) with the control simulation. Vertical dashed lines represent the time of TCG in ensemble member 10 and the control; member 7 undergoes TCG at 12/1800.

also having lower area-averaged MSLP. This correlation, however, has been influenced by the outlying members, although the general negative trend still exists within the ensemble cluster. As more ensemble members strengthen, the negative correlation becomes more robust, with a Pearson's correlation of −0.937 (Fig. 11b). Such a strong negative correlation implies that the fast developers (e.g., those undergoing TCG) have prominent upper-tropospheric warming. This is supported by the increased spread in both area-averaged upper-tropospheric temperatures and MSLP, as a large cluster of members has area-averaged MSLP below 1007 hPa and 400–150-hPa layer-averaged temperatures of above −37°C. A clear schism between the developers and nondevelopers at 12/0600 can easily be identified, as indicated by the vertical and horizontal dashed lines in Fig. 11b. Thus, the impact of upper-level warming on MSLP changes can be seen from the entire ensemble, with notable differences between faster- and slower (or non)-developing members. This is especially evident at 12/0600, as a cluster of members undergo or are in the process of TCG.

The difference in upper-tropospheric warming between the members is also consistent with observations taken during PREDICT, although the warming may sometimes occur in the midtroposphere (Zhang and Zhu 2012). Komaromi (2013) investigated composite dropsondes during PREDICT for developing and nondeveloping storms in comparison to the mean temperature profile from the campaign. The work shows that 1.0°–2.0°C warm anomalies in developing storms occur 0–24 h prior to TCG within 200 km of the storm center. The work also states that negative anomalies from 0.5° to 1.0°C occur for nondeveloping storms when compared to the mean profile, which are also consistent with those shown in Fig. 9.

b. *Differences in the outflow layer*

Given the obvious differences in the upper-tropospheric warming, it is worthwhile to examine the characteristics of how the warm air is able to accumulate in the developers versus the nondevelopers. Cecelski and Zhang (2013) demonstrated that the accumulation of the upper-level warmth results from a storm-scale outflow developing beyond L_R, within which the velocity field tends to adjust to the mass field, with significant reduction in energy dispersion by gravity waves. Further, high VWS in the warming layer inhibits the formation of the upper-level warming (Zhang and Zhu 2012), as the warming is "sheared apart."

To investigate the key differences in the outflow layer, Fig. 12 shows the 100 km × 100 km area-averaged L_R, 400–150-hPa layer-averaged divergence, and 400–150-hPa layer-averaged VWS for the same time period as Fig. 9. The upper-level warming seen for member 10 (Figs. 9, 10) becomes a system-scale feature due to a significant reduction in L_R below 800 km, a potent divergent

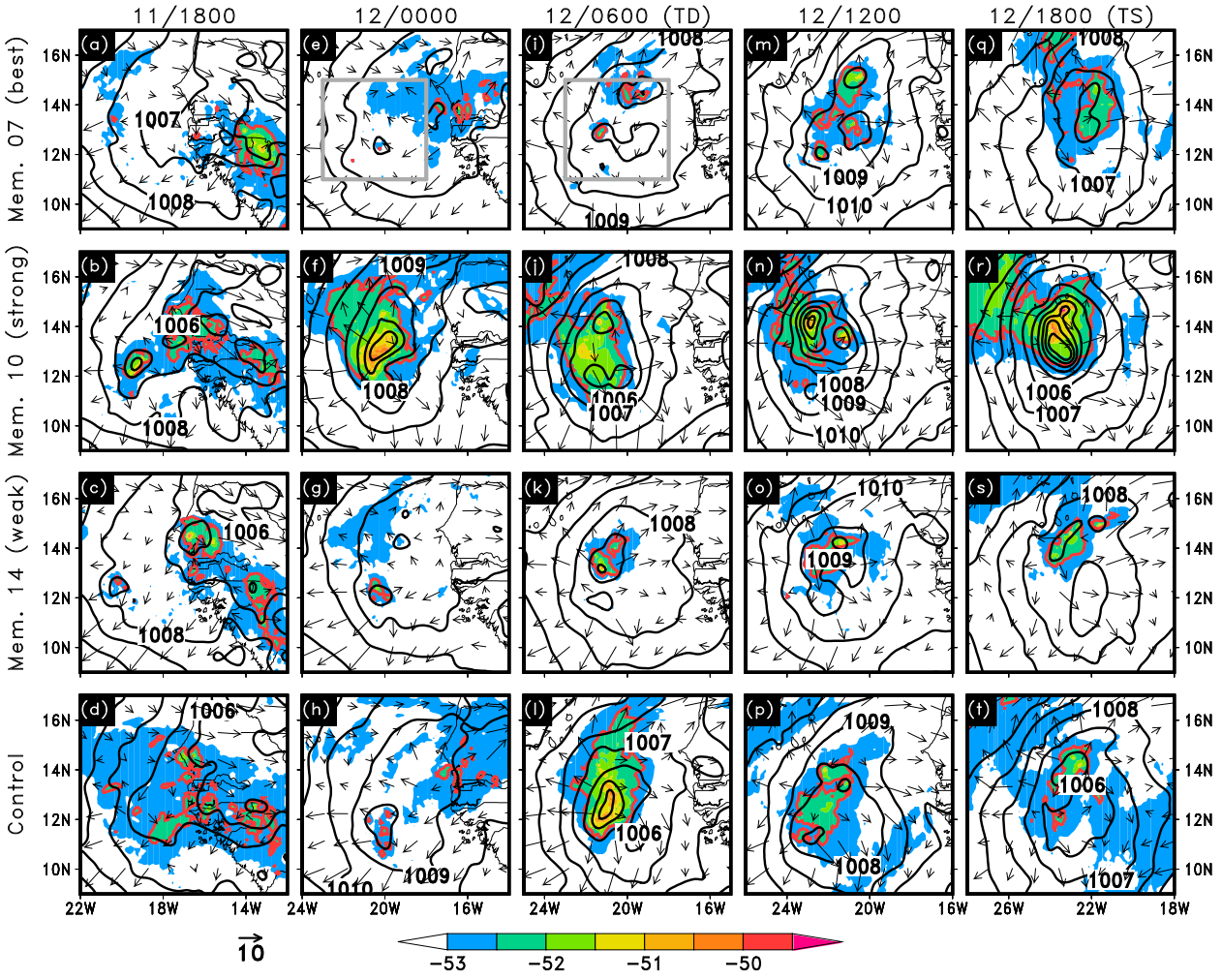

FIG. 10. Comparison of the 200-hPa temperature (color shaded, °C), MSLP (contoured at intervals of 1 hPa), and comoving wind vectors (reference vector is 10 m s^{-1}) from ensemble members (first row) 7, (second row) 10, (third row) 14, and (fourth row) the control simulation that are valid at (a)–(d) 1800 UTC 11 Sep and (e)–(h) 0000, (i)–(l) 0600, (m)–(p) 1200, and (q)–(t) 1800 UTC 12 Sep, respectively. The −52.5°C isotherm at 200 hPa is contoured in thick red to show areal changes of the warming with time. The gray boxes in (e),(i) represent the area used for the averages in Figs. 11 and 13. Data from the 9-km-resolution simulation were used for the analysis.

outflow extending beyond L_R, and low VWS in the warming layer (red lines, Figs. 12a–c). As the upper-tropospheric warming takes place, local static stability is reduced, causing L_R to shrink. As will be shown later, the large divergent outflow in member 10 results from the maintenance of deep convection near the AEW pouch center and its upscale aggregation into an MCS. Unlike member 10, the nondeveloper (member 14) shows minimal reduction in L_R, weak divergent outflow, and a steady increase in 400–150-hPa layer VWS to above 18 m s^{-1} (blue lines, Figs. 12a–c). Given the combination of these characteristics, it is not surprising that significant warmth could not accumulate on the storm scale. It is very likely that the weak warming seen for member 14 in Fig. 9c diminished as a result of the large increase in the outflow layer VWS, in a fashion similar to the control. Thus, the system-scale warming is reliant on the outflow layer being cooperative with weak VWS. Otherwise, even if a storm-scale outflow beyond L_R is present, the warming will be "torn apart" by the VWS. An interesting topic for future work of ours will be *why* the VWS differences exist, as the results herein do not elucidate such differences.

Further elaborating on the upper-tropospheric warming in the outflow layer, Fig. 13 compares the area-averaged 400–150-hPa layer-averaged relative divergence and temperature between each ensemble member at 12/0000 and 12/0600. A clear, positive correlation (with a correlation coefficient of 0.733) exists at 12/0000, with members having greater divergence in the 400–150-hPa layer and

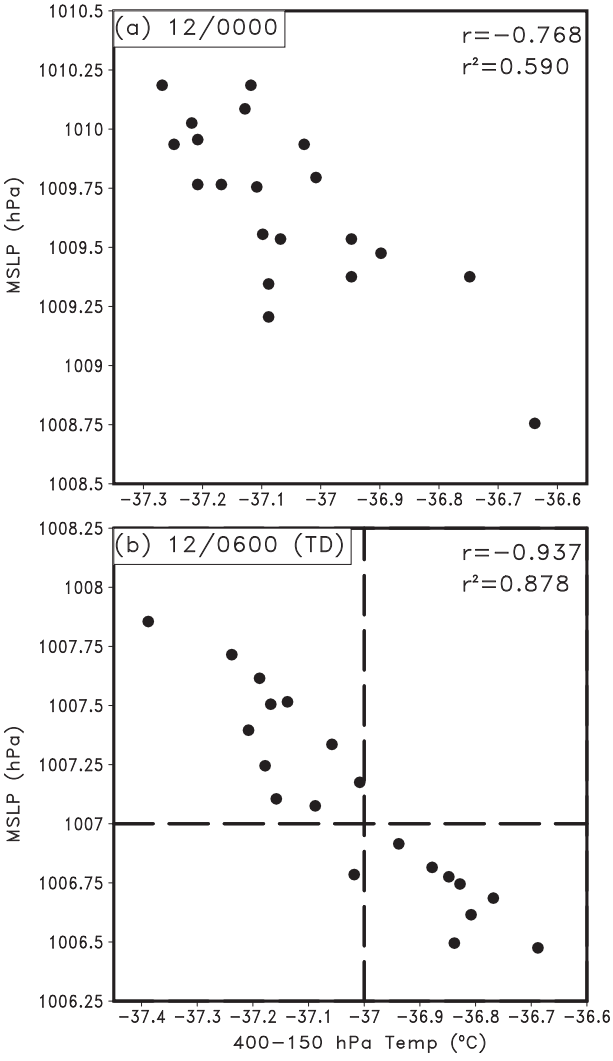

FIG. 11. Scatterplots of the 500 km × 500 km area-averaged 400–150-hPa layer-averaged temperature (°C; x axis) vs MSLP (hPa; y axis) from each ensemble member at (a) 0000 and (b) 0600 UTC 12 Sep (see Figs. 10e and 10i for the areas used for averaging). The Pearson's correlation coefficient (r) and the coefficient of determination (r^2) are calculated at each time and are listed. The vertical and horizontal dashed lines in (b) represent the schism between fast- and slow-developing ensemble members. Data from the 3-km-resolution simulation were used in the averaging.

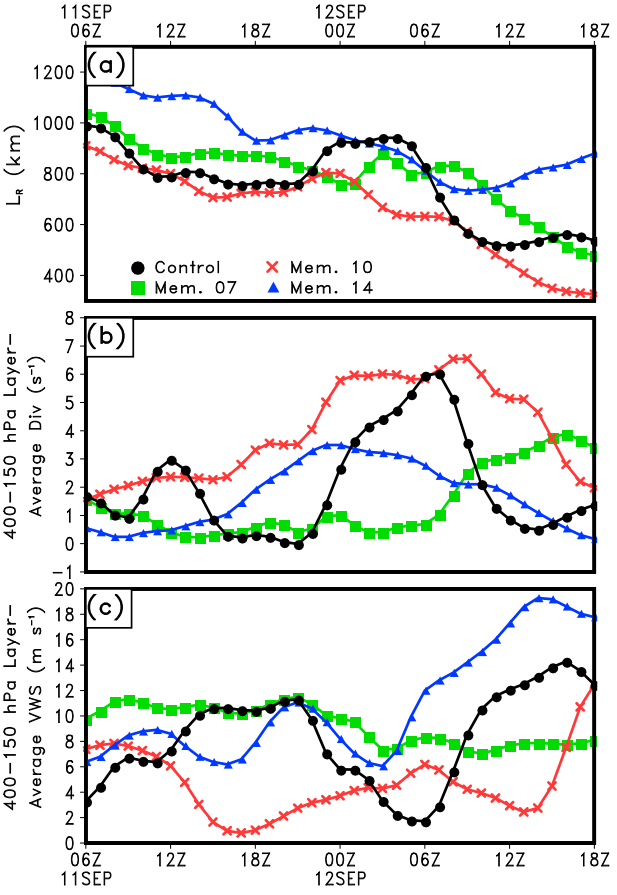

FIG. 12. Time series (0600 UTC 11 Sep–1800 UTC 12 Sep) of the 100 km × 100 km area-averaged (a) Rossby radius of deformation {$L_R = NH/\eta$, where η is the 1000–400-hPa layer-averaged absolute vorticity; $N = [(g/\overline{\theta})/(d\theta/dz)]^{1/2}$ is calculated using the area-averaged 1000-hPa potential temperature ($\overline{\theta}$), the vertical differential potential temperatures and heights between 150 and 1000 hPa ($d\theta/dz$), and g is the gravitational constant; and H is calculated using $H = R\overline{T}/g$, where $\overline{T}$ is the average temperature between 1000 and 150 hPa, and R is the gas constant for dry air}; (b) 400–150-hPa layer-averaged divergence (s^{-1}); and (c) 400–150-hPa layer-averaged VWS (m s^{-1}) from the selected four members using 3-km-resolution domain data.

warmer area-averaged upper-tropospheric temperatures. A very similar pattern, though an opposite correlation, can be seen when comparing Fig. 13a with Fig. 11a, alluding to the interconnectedness of the parameters investigated. Most ensemble members have area-averaged divergence below $1.6 \times 10^{-5}\,s^{-1}$ in conjunction with upper-tropospheric temperatures below −37°C. By 12/0600, a more definitive ensemble spread occurs as fast developers depict a more pronounced divergent outflow in addition to the warmer upper-tropospheric temperatures (Fig. 13b). The difference between slower- and faster-developing members can also be easily identified by the vertical and horizontal dashed lines in Fig. 13b, marking the intersection of −37°C upper-tropospheric temperatures and $2.3 \times 10^{-5}\,s^{-1}$ divergence. These results support our initial findings that a prominent divergent outflow aids in the expansion of the upper-tropospheric warming over a meso-α-scale area as L_R shrinks due to the reduced static stability in the upper troposphere.

c. *Differences in convective initiation*

The development of persistent deep convection can help precondition the tropospheric column with sufficient

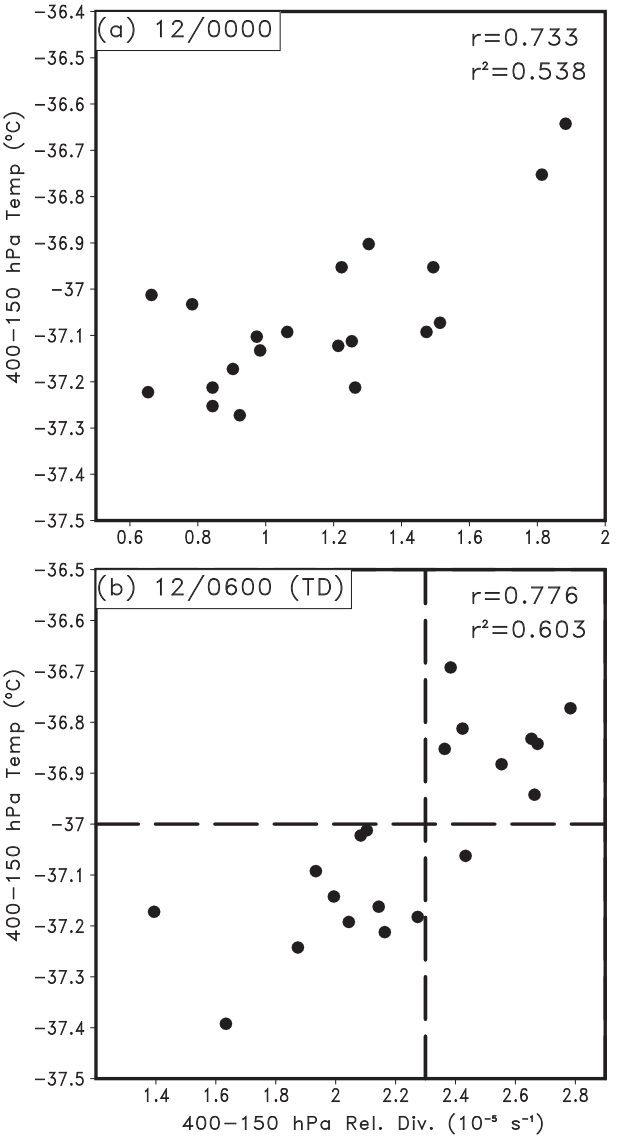

FIG. 13. As in Fig. 11, but for 400–150-hPa layer-averaged relative divergence ($\times 10^{-5}$ s^{-1}; x axis) and 400–150-hPa layer-averaged temperature (°C; y axis).

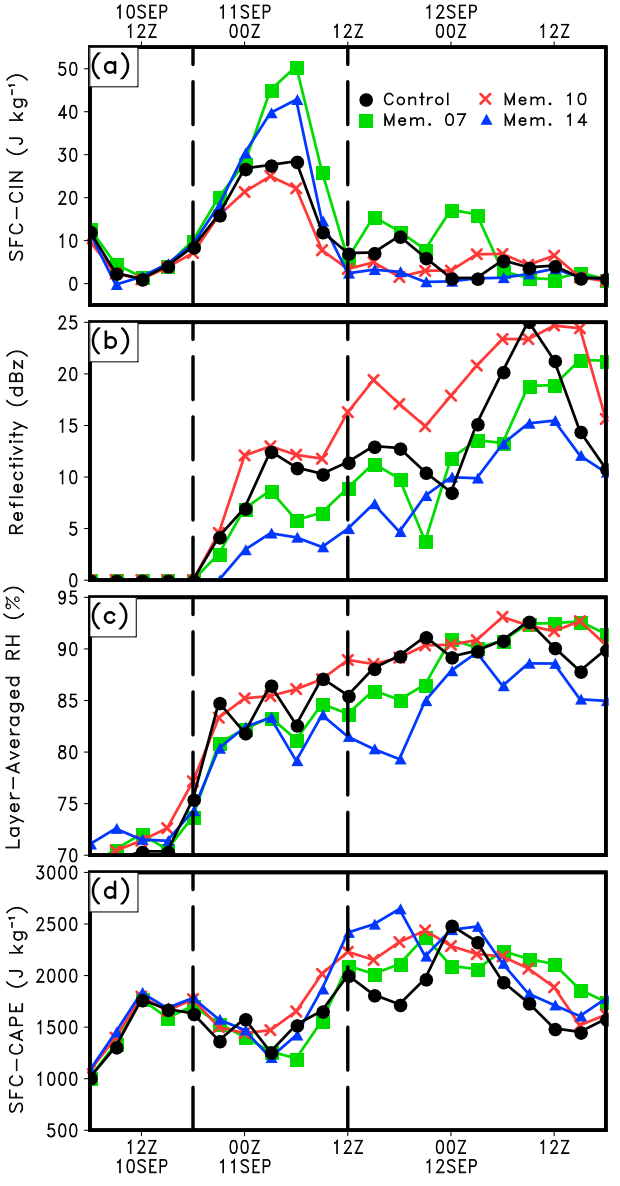

FIG. 14. Time series of (a) surface-based CIN (J kg^{-1}), (b) simulated composite radar reflectivity (dBZ), (c) 550–500-hPa layer-averaged RH (%), and (d) surface-based CAPE (J kg^{-1}) that are each averaged over an area of 200 km × 200 km around the storm center from ensemble members 7 (green, best), 10 (red, strongest), 14 (blue, weakest), and the control simulation (black) valid from 0600 UTC 10 Sep to 1800 UTC 12 Sep from the 9-km-resolution domain. The vertical dashed lines encompass the period where convective development was limited in all members.

moisture, an important factor for the occurrence of TCG within an AEW (Hopsch et al. 2010). TCG has also been shown to have ties to deep convection and its area coverage by Sippel and Zhang (2008) through high-tropospheric moisture content and CAPE. In addition, upper-level warming development (Figs. 9, 10) relies on persistent deep convection and a storm-scale outflow within the AEW (Cecelski and Zhang 2013; Zhang and Zhu 2012). The latent heating in the upper troposphere due to deposition and freezing has been shown to be related to the intensification and aggregation of deep convection [or convective bursts (CBs) through associated low-level vortical circulations] into an MCS along the low-level AEW critical latitude (Cecelski and Zhang 2013). As the MCS becomes organized, the storm-scale outflow expands beyond the shrinking L_R, enabling the accumulation of meso-α-scale warming in the upper troposphere. Figure 14 shows the time series of surface-based convective inhibition (CIN), simulated composite radar reflectivity, 550–500-hPa layer-averaged relative humidity,

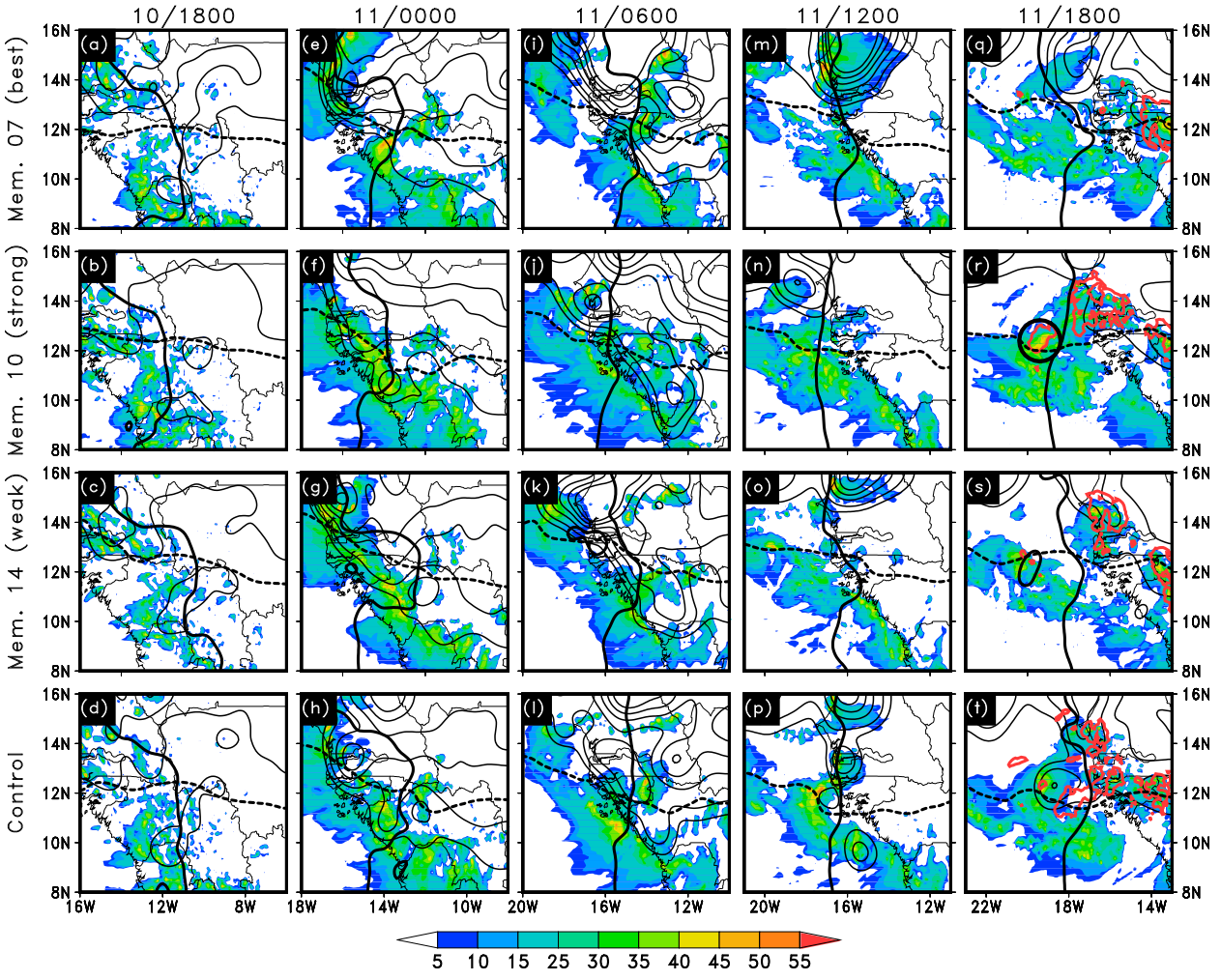

FIG. 15. Comparison of the composite radar reflectivity (shaded, dBZ) and surface-based CIN (contoured at 10, 20, 40, 60, 80, and 100 J kg^{-1}) from ensemble members (first row) 7, (second row) 10, (third row) 14, and (fourth row) the control simulation valid at (a)–(d) 1800 UTC 10 Sep and (e)–(h) 0000, (i)–(l) 0600, (m)–(p) 1200, and (q)–(t) 1800 UTC 11 Sep, respectively. The 600-hPa AEW trough axis and critical latitude are shown with the thick solid and dashed lines, respectively. The −52.5°C isotherm at 200 hPa is contoured in thick red at 1800 UTC 11 Sep in (q)–(t) to demonstrate the relationship between the warming and deep convection. The circle in (r) encompasses the location of the first closed MSLP contour from member 10. Data from the 9-km-resolution domains were used.

and surface-based CAPE that are area averaged around each members' respective storm center. In addition, Fig. 15 shows the spatial distribution of composite radar reflectivity and surface-based CIN. Further, Figs. 15q–t show the 200-hPa −52.5°C isotherm valid at 11/1800, the time at which member 10 first develops a meso-β-scale P_{MIN}.

The surface-based CIN (Fig. 14a) shows one distinct period of member differences between 10/1800 and 11/1200, as encompassed by the dashed lines. Before 10/1800, CIN values are agreed upon in all members, averaging around 10 J kg^{-1} (Fig. 14a) with no convection in the core region (Fig. 14b). CIN quickly increases in members 7 and 14 after 10/1800 (green and blue lines in Fig. 14a) reaching 55 and 45 J kg^{-1}, respectively, at 11/0600. In contrast, member 10 has a much slower increase in CIN values, reaching 25 J kg^{-1} at 11/0600, nearly half that of the other members. The development of CIN in all members takes place to the north and west of each member's AEW pouch center between 10/1800 and 11/0600 (Figs. 15a–l), reaching a maximum just before sunrise when the nocturnal inversion is the strongest (11/0600). Such a finding alludes to the possibility that radiational cooling is contributing to the enhanced CIN values. The CIN suppresses convective development between 11/0000 and 11/0900 in all ensemble members and the control, with average composite radar reflectivity returns below 15 dBZ near the storm centers (Figs. 14b, 15).

After 11/0600, all members show a large reduction of CIN (Fig. 14a), with member 10 beginning to initiate

more convection near the storm center (Fig. 15n). In general, the suppression of deep convection due to CIN during the 18-h period of 10/1800 and 11/1200 has a lasting impact on the spatial coverage of convection near the storm centers of all the members. At local noon (i.e., 11/1200), vertical mixing of the PBL tends to remove any possible nocturnal inversion. However, the larger the CIN (e.g., inversion), the longer it takes to erode, and thus the members with greater CIN (members 7 and 14) show the suppression of new convective development (Figs. 15m,o,q,s). Member 10 with its weaker CIN near the AEW pouch center reinvigorates the MCS off the coastline between 11/1200 and 11/1800 (Figs. 15n,r), in a fashion similar to the control (Figs. 15p, t). Delayed convective initiation persists in the nondeveloper (member 14), with average composite reflectivity returns well below member 10 from 11/1800 to the end of the simulation (Fig. 14b). The development of the meso-β-scale P_{MIN} in member 10 is found where the strongest reflectivity returns over water occur, in a region characterized by temperatures greater than -52.5°C at 200 hPa (circled area in Fig. 15r). Such a finding is consistent with the results discussed previously with respect to the outflow layer (see red lines, Figs. 12a–c).

The midtropospheric moisture content also exhibits differences between the members, as shown by the layer-averaged 550–500-hPa relative humidity (RH; Fig. 14c). As convection develops between 10/1800 and 11/000 (Figs. 14b, 15), all members show an increase in layer-averaged RH values with member 10 having the largest increase of nearly 10%. A slow (but variable) increase in the layer-averaged RH occurs between 11/0000 and 11/1200 as new convection struggles to develop (Figs. 14a,c). The differences in RH between the members become most notable between 11/1200 and 12/0000, as convective development increases and CIN is reduced. Member 10 shows a consistent increase in midlevel RH to above 90% by 12/0000, while members 7 and 14 show a delayed response in the midlevel moistening directly after 11/1200. This delay in development until roughly 11/1800 can be attributed to having to overcome larger CIN in the previous 12-h period (Figs. 14, 15). After 12/0000, every member except for member 14 has sufficient midlevel moisture with RH values nearing 90% (Fig. 14c). Such a difference is readily explained by the lack of convective development near the storm center in member 14, as seen in Figs. 15b and 14.

Surprisingly, surface-based CAPE exhibits little differences between the developers and nondevelopers. This result does not agree with that of Komaromi (2013), who found that nondeveloping storms had substantially larger CAPE than developing storms when calculated from composite soundings during the PREDICT campaign. Our findings also somewhat disagree with Sippel and Zhang (2008), who noted CAPE as an important initial condition for the early 6–12-h period of integration in developers, in contrast to the findings of Komaromi (2013). We state that the results disagree "somewhat" with Sippel and Zhang (2008) since they do explicitly mention that (i) their results are specific to the storm investigated; (ii) their results do not imply that CAPE is directly correlated to occurrence of TCG; and (iii) they believe it is possible for CAPE to speed up TCG, given a favorable large-scale environment. Even so, CAPE is only a measure of energy *available* to the parcel and may be useful after overcoming CIN. Thus, we believe that CAPE differences are secondary to the ability to generate and sustain deep convection, which relies on reduced CIN and development along the low-level AEW critical latitude near the AEW pouch center (Dunkerton et al. 2009; Cecelski and Zhang 2013). Overall though, the general idea from Sippel and Zhang (2008) that convective development and coverage are important for TCG is agreed upon with our findings. This overarching characteristic of developing disturbances is also supported by Hopsch et al. (2010).

Our results indicate that the predisposition of larger CIN in members 7 and 14 suppresses convective development and thus the vertical moisture transport needed to precondition the atmosphere prior to TCG. This result is consistent with Hopsch et al. (2010), who notes that nondeveloping AEWs are more likely to have drier air in the mid- and upper levels. The above results allude to the need for fast-developing waves (Hopsch et al. 2010) to also have lower CIN in close proximity to their pouch center, so that convection can develop and persistently moisten the midtroposphere. These CIN values could possibly tie to the time of day for the coastline passage, which if at night, would enhance the CIN due to the development of a nocturnal inversion. The diurnal nature of convection has been shown to be linked to TCG by Ventrice et al. (2012a) and thus, similar variations in CIN could be the limiting factor of convective development. Overall, the strongest developer (member 10) had less CIN to overcome early in the simulation, allowing for the faster development of a persistent MCS. This in turn preconditions the mid- and upper troposphere with moisture and also allows for the faster development and expansion of the storm-scale outflow and thus upper-tropospheric warming.

5. Summary and conclusions

In this study, we examine the predictability of the genesis of Hurricane Julia (2010) using a suite of WRF-LETKF ensemble simulations and the differences between them.

Results show that the TCG of the simulated Julia is highly predictable with 18 out of 20 members having P_{MIN} deeper than the NHC estimated 1007 hPa at 12/0600. Our work herein focuses on the following three factors for TCG: convective initiation, the upper-level outflow layer, and upper-level warming. They are strongly tied together since persistent deep convection and its maturation along the low-level AEW critical latitude during TCG allows for (i) the development of the storm-scale outflow, (ii) a reduction of L_R, and (iii) the depositional heating of the upper troposphere.

The variability of the simulated genesis from the 20 ensemble members is analyzed to gain insight into the important parameters involved in TCG. Results indicate that the strongest member has the most prominent upper-level warming over a larger spatial area prior to and at TCG, which induces similar-sized meso-α MSLP falls and the development of a meso-β surface low into a TD. In particular, the meso-β-scale surface low is consistently located with the warmest air in the upper troposphere, demonstrating the importance of maintaining the upper-level warm air for hydrostatically causing surface pressure falls. Clearly, results indicate that the opposite is true for the weakest member. Depositional growth of ice particles appears to play an important role in generating upper-level warming, which is supported by the findings of the strongest member having cloud ice content nearly double that of weaker members. In order for the upper-level warming to form, persistent deep convection must intensify and aggregate into an MCS through the associated low-level vortical circulations along the low-level AEW critical latitude. The aggregation of deep convection results in the development of the storm-scale outflow beyond L_R, enabling the accumulation and expansion of the warming air. In addition, a decrease of L_R in the strongest developer aids in the accumulation of warmth, while the opposite is true for the nondeveloper. Results suggest that the reduction of L_R stems from a decrease in static stability in the upper troposphere due to the depositional heating. Further, significant differences in the strength of upper-tropospheric VWS occur between the strongest developer and nondeveloper. These differences allude to large upper-tropospheric VWS inhibiting the growth of the upper-level warming and thus the inability to create a system-scale upper-level warm core. Further work needs to be done to investigate why such significant differences in VWS occur. Our results suggest that while the marsupial pouch paradigm provides a theoretical construct to identify the ideal location for TCG, it may not succeed in tracing the subsequent development without examining upper-level processes.

Initiation of deep convection near the AEW pouch center is found to be tied to the magnitude CIN earlier in the simulations. The member with weaker CIN early in the simulation shows the faster development of convection after coastal passage and has the faster-developing TD. This is consistent with previous work such that fast-developing waves have higher midtropospheric moisture content and stronger convection during coastal passage. Supplementing this idea, the faster development and aggregation of deep convection over the ocean allows for the upper-level warming to intensify and expand faster with time, inducing MSLP falls earlier in comparison to the other members. Thus, we believe that fast-developing AEWs might also have an appreciable difference in the magnitude of CIN near the pouch center during coastal passage. Little differences in surface-based CAPE are found between developers and nondevelopers, indicating that this parameter may be secondary to CIN magnitude prior to TCG, since parcels cannot use CAPE before CIN is overcome.

In conclusion, we may state that the fundamental ensemble member differences for the TCG of Julia involve convective initiation and depth near the core region and the development of storm-scale outflow and upper-tropospheric warming. Given that the synoptic-scale environment was favorable for TCG through sufficient SSTs and low large-scale tropospheric VWS, the slight differences in the initiation and persistence of storm-scale deep convection near the AEW pouch center could be responsible for the occurrence of TCG. While the development of upper-level warming and a storm-scale outflow has been argued as symptoms of a developing TC, we propose that they are actually precursors to TCG, especially when such fields are on the meso-β-scale in character during the early stages of TCG. It is not until these features become storm scale that system-wide balance starts to occur and the fundamental ideas for the intensification and balance of an ''axis-symmetric'' TC can be applied. We do realize, however, that the parent AEW can be considered near axis-symmetric, in balance, and is characterized by mixed baroclinic–barotropic instability. Regardless, it is evident that TCG is riddled with the processes that are inherently asymmetric and evolve to become axis-symmetric as upscale (vortical) aggregation occurs, a common theme addressed in numerous previous studies. The ''chicken or the egg'' logic applied to the development of P_{MIN} can simply be disputed by the hydrostatic MSLP falls resultant from upper-level warming. Taking away the warming (e.g., by strong VWS in the outflow layer), MSLP falls will not occur and TCG might not take place. To test this further, we will conduct a sensitivity study by changing depositional latent heating in the microphysics scheme of the WRF model. Further, we plan to provide a more holistic and statistical measure of the ensemble forecasts by conducting

an ensemble sensitivity analysis on MSLP changes, which will appear in a forthcoming journal article.

Acknowledgments. This work was supported by NASA Headquarters under the NASA Earth and Space Science Fellowship Program Grant NNX11AP29H. Model simulations were performed at the NASA High-End Computing (HEC) Program through the NASA Center for Climate Simulation (NCCS) at Goddard Space Flight Center. The ERA-Interim and NCEP PREPBUFR data for this study were from the Research Data Archive (RDA) maintained by the Computational and Information Systems Laboratory (CISL) at the National Center for Atmospheric Research, which is sponsored by the National Science Foundation. Satellite data were provided by the Cooperative Institute for Meteorological Satellite Studies (CIMSS) Tropical Cyclone Image Archive, University of Wisconsin.

APPENDIX

WRF–LETKF System Details

The code used for the WRF–LETKF data assimilation system was developed by Miyoshi (2005) and adapted for WRF by MK12. A four-dimensional ensemble Kalman filter (4D-EnKF; Hunt et al. 2004) allows for the system to ingest asynchronous observations and includes spatial covariance localization with a physical distance (Miyoshi et al. 2007) as well as temporal covariance localization. The assimilation cycle in the WRF–LETKF system uses observational data produced every 6 h (0000, 0600, 1200, and 1800 UTC) in the PREPBUFR format (Keyser 2013) from NCEP's GDAS. The PREPBUFR data are used within a 6-h window centered on the analysis time with the observation time rounded to the hour for hourly input into the 4D-LETKF (MK12). WRF first-guess forecasts are integrated forward for 9-h periods, beginning 6 h prior to the analysis time. The system conducts the assimilation using the following three-dimensional prognostic variables: temperature (T), water vapor mixing ratio (q_v), pressure (P), geopotential height (ph), and wind components (u, v, and w). Additionally, surface pressure (ps), 2-m temperature (T_2), and 2-m water vapor mixing ratio (q_2) are used in the observational operators. Similar localization parameters to those of MK12 are used in the cycle, including a 400-km horizontal, 0.4-ln (P) vertical, and 3-h time localization parameter. The choice for these values stems from the success of assimilating real-time observations in previous studies (Miyoshi et al. 2010). This cycle does not use adaptive covariance inflation (Miyoshi 2011), but uses a fixed, domain-constant, 20% covariance multiplicative inflation (e.g., a 1.20 inflation parameter). This global constant is used since this method closely resembles the results of the adaptive inflation technique for a 96-h cycle (see Fig. 3 of MK12).

REFERENCES

Cecelski, S. F., and D.-L. Zhang, 2013: Genesis of Hurricane Julia (2010) within an African easterly wave: Low-level vortices and upper-level warming. *J. Atmos. Sci.,* **70,** 3799–3817, doi:10.1175/JAS-D-13-043.1.

Chen, H., and D.-L. Zhang, 2013: On the rapid intensification of Hurricane Wilma (2005). Part II: Convective bursts and the upper-level warm core. *J. Atmos. Sci.,* **70,** 146–172, doi:10.1175/JAS-D-12-062.1.

Dudhia, J., 1989: Numerical study of convection observed during the winter monsoon experiment using a mesoscale two-dimensional model. *J. Atmos. Sci.,* **46,** 3077–3107, doi:10.1175/1520-0469(1989)046<3077:NSOCOD>2.0.CO;2.

Dunkerton, T. J., M. T. Montgomery, and Z. Wang, 2009: Tropical cyclogenesis in a tropical wave critical layer: Easterly waves. *Atmos. Chem. Phys.,* **9,** 5587–5646, doi:10.5194/acp-9-5587-2009.

Emanuel, K. A., J. D. Neelin, and C. S. Bretherton, 1994: On large-scale circulations in convecting atmospheres. *Quart. J. Roy. Meteor. Soc.,* **120,** 1111–1144, doi:10.1002/qj.49712051902.

Enomoto, T., M. Hattori, T. Miyoshi, and S. Yamane, 2010: Precursory signals in analysis ensemble spread. *Geophys. Res. Lett.,* **37,** L08804, doi:10.1029/2010GL042723.

Hendricks, E. A., M. T. Montgomery, and C. A. Davis, 2004: The role of vortical hot towers in the formation of Tropical Cyclone Diana (1984). *J. Atmos. Sci.,* **61,** 1209–1232, doi:10.1175/1520-0469(2004)061<1209:TROVHT>2.0.CO;2.

Hong, S.-Y., J. Dudhia, and S.-H. Chen, 2004: A revised approach to ice microphysical processes for the bulk parameterization of clouds and precipitation. *Mon. Wea. Rev.,* **132,** 103–120, doi:10.1175/1520-0493(2004)132<0103:ARATIM>2.0.CO;2.

Hopsch, S. B., C. D. Thorncroft, and K. R. Tyle, 2010: Analysis of African easterly wave structures and their role in influencing tropical cyclogenesis. *Mon. Wea. Rev.,* **138,** 1399–1419, doi:10.1175/2009MWR2760.1.

Houze, R. A., W.-C. Lee, and M. M. Bell, 2009: Convective contribution to the genesis of Hurricane Ophelia (2005). *Mon. Wea. Rev.,* **137,** 2778–2800, doi:10.1175/2009MWR2727.1.

Hunt, B. R., and Coauthors, 2004: Four-dimensional ensemble Kalman filtering. *Tellus,* **56A,** 273–277, doi:10.1111/j.1600-0870.2004.00066.x.

——, E. J. Kostelich, and I. Szunyogh, 2007: Efficient data assimilation for spatiotemporal chaos: A local ensemble transform Kalman filter. *Physica D,* **230,** 112–126, doi:10.1016/j.physd.2006.11.008.

Kain, J. S., 2004: The Kain–Fritsch convective parameterization: An update. *J. Appl. Meteor.,* **43,** 170–181, doi:10.1175/1520-0450(2004)043<0170:TKCPAU>2.0.CO;2.

Keyser, D., 2013: PREPBUFR processing at NCEP. National Centers for Environmental Prediction Tech. Rep. [Available online at http://www.emc.ncep.noaa.gov/mmb/data_processing/prepbufr.doc/document.htm.]

Komaromi, W., 2013: An investigation of composite dropsonde profiles for developing and nondeveloping tropical waves

during the 2010 PREDICT field campaign. *J. Atmos. Sci.,* **70,** 542–558, doi:10.1175/JAS-D-12-052.1.

Miyoshi, T., 2005: Ensemble Kalman filter experiments with a primitive-equation global model. Ph.D. thesis, University of Maryland, 197 pp.

——, 2011: The Gaussian approach to adaptive covariance inflation and its implementation with the local ensemble transform Kalman filter. *Mon. Wea. Rev.,* **139,** 1519–1535, doi:10.1175/2010MWR3570.1.

——, and M. Kunii, 2012: The local ensemble transform Kalman filter with the weather research and forecasting model: Experiments with real observations. *Pure Appl. Geophys.,* **169,** 321–333, doi:10.1007/s00024-011-0373-4.

——, S. Yamane, and T. Enomoto, 2007: Localizing the error covariance by physical distances within a local ensemble transform Kalman filter (LETKF). *SOLA,* **3,** 89–92, doi:10.2151/sola.2007-023.

——, Y. Sato, and T. Kadowaki, 2010: Ensemble Kalman filter and 4D-Var intercomparison with the Japanese operational global analysis and prediction system. *Mon. Wea. Rev.,* **138,** 2846–2866, doi:10.1175/2010MWR3209.1.

Mlawer, E. J., S. J. Taubman, P. D. Brown, M. J. Iacono, and S. A. Clough, 1997: Radiative transfer for inhomogeneous atmospheres: RRTM, a validated correlated-*k* model for the longwave. *J. Geophys. Res.,* **102,** 16 663–16 682, doi:10.1029/97JD00237.

Montgomery, M. T., M. E. Nicholls, T. A. Cram, and A. B. Saunders, 2006: A vortical hot tower route to tropical cyclogenesis. *J. Atmos. Sci.,* **63,** 355–386, doi:10.1175/JAS3604.1.

——, L. L. Lussier III, R. W. Moore, and Z. Wang, 2010: The genesis of Typhoon Nuri as observed during the tropical cyclone structure 2008 (TCS-08) field experiment—Part 1: The role of the easterly wave critical layer. *Atmos. Chem. Phys.,* **10,** 9879–9900, doi:10.5194/acp-10-9879-2010.

——, and Coauthors, 2012: The Pre-Depression Investigation of Cloud-Systems in the Tropics (PREDICT) experiment: Scientific basis, new analysis tools and some first results. *Bull. Amer. Meteor. Soc.,* **93,** 153–172, doi:10.1175/BAMS-D-11-00046.1.

Noh, Y. W., W. G. Cheon, S. Y. Hong, and S. Raasch, 2003: Improvement of the K-profile model for the planetary boundary layer based on large eddy simulation data. *Bound.-Layer Meteor.,* **107,** 401–427, doi:10.1023/A:1022146015946.

Reynolds, R. W., T. M. Smith, C. Lui, D. B. Chelton, K. S. Casey, and M. G. Schlax, 2007: Daily high-resolution blended analyses for sea surface temperature. *J. Climate,* **20,** 5473–5496, doi:10.1175/2007JCLI1824.1.

Sippel, J. A., and F. Zhang, 2008: The probabilistic analysis of the dynamics and predictability of tropical cyclogenesis. *J. Atmos. Sci.,* **65,** 3440–3459, doi:10.1175/2008JAS2597.1.

——, J. W. Nielsen-Gammon, and S. E. Allen, 2006: The multiple-vortex nature of tropical cyclogenesis. *Mon. Wea. Rev.,* **134,** 1796–1814, doi:10.1175/MWR3165.1.

Skamarock, W. C., J. B. Klemp, J. Dudhia, D. O. Gill, D. M. Barker, W. Wang, and J. G. Powers, 2005: A description of the advanced research WRF version 2. NCAR Tech. Note NCAR/TN-468+STR, 88 pp. [Available online at http://www.mmm.ucar.edu/wrf/users/docs/arw_v2.pdf.]

Snyder, A. D., Z. Pu, and Y. Zhu, 2010: Tracking and verification of east Atlantic tropical cyclone genesis in the NCEP global ensemble: Case studies during the NASA African monsoon multidisciplinary analyses. *Wea. Forecasting,* **25,** 1397–1411, doi:10.1175/2010WAF2222332.1.

Thompson, G., P. R. Field, R. M. Rasmussen, and W. D. Hall, 2008: Explicit forecasts of winter precipitation using an improved bulk microphysics scheme. Part II: Implementation of a new snow parameterization. *Mon. Wea. Rev.,* **136,** 5095–5115, doi:10.1175/2008MWR2387.1.

Ventrice, M. J., C. D. Thorncroft, and M. A. Janiga, 2012a: Atlantic tropical cyclogenesis: A three-way interaction between an African easterly wave, diurnally varying convection, and a convectively coupled atmospheric Kelvin wave. *Mon. Wea. Rev.,* **140,** 1108–1124, doi:10.1175/MWR-D-11-00122.1.

Wang, Z., M. T. Montgomery, and T. J. Dunkerton, 2010a: Genesis of pre–Hurricane Felix (2007). Part I: The role of the easterly wave critical layer. *J. Atmos. Sci.,* **67,** 1711–1729, doi:10.1175/2009JAS3420.1.

Zhang, D.-L., and N. Bao, 1996: Oceanic cyclogenesis as induced by a mesoscale convective system moving offshore. Part II: Genesis and thermodynamic transformation. *Mon. Wea. Rev.,* **124,** 2206–2226, doi:10.1175/1520-0493(1996)124<2206:OCAIBA>2.0.CO;2.

——, and L. Zhu, 2012: Roles of upper-level processes in tropical cyclogenesis. *Geophys. Res. Lett.,* **39,** L17804, doi:10.1029/2012GL053140.